

LETTER TO THE EDITOR

Silicon in the dust formation zone of IRC +10216 as observed with PACS and SPIRE on board Herschel [★]

L. Decin^{1,2}, J. Cernicharo³, M.J. Barlow⁴, P. Royer¹, B. Vandenbussche¹, R. Wesson⁴, E.T. Polehampton^{5,6}, E. De Beck¹, M. Agúndez^{3,10}, J.A.D.L. Blommaert¹, M. Cohen⁸, F. Daniel³, W. De Meester¹, K. Exter¹, H. Feuchtgruber¹¹, J.P. Fonfría⁷, W.K. Gear¹², J.R. Goicoechea³, H.L. Gomez¹², M.A.T. Groenewegen¹³, P.C. Hargrave¹², R. Huygen¹, P. Imhof¹⁴, R.J. Ivison¹⁵, C. Jean¹, F. Kerschbaum¹⁷, S.J. Leeks⁵, T. Lim⁵, M. Matsuura^{4,18}, G. Olofsson¹⁶, T. Posch¹⁷, S. Regibo¹, G. Savini⁴, B. Sibthorpe¹⁵, B.M. Swinyard⁵, B. Tercero³, C. Waelkens¹, D.K. Witherick⁴, and J.A. Yates⁴

(Affiliations can be found after the references)

Received / accepted

Abstract

The interstellar medium is enriched primarily by matter ejected from evolved low and intermediate mass stars. The outflows from these stars create a circumstellar envelope in which a rich gas-phase and dust-nucleation chemistry takes place. We observed the nearest carbon-rich evolved star, IRC +10216, using the PACS (55–210 μm) and SPIRE (194–672 μm) spectrometers on board Herschel. We find several tens of lines from SiS and SiO, including lines from the v=1 vibrational level. For SiS these transitions range up to J=124–123, corresponding to energies around 6700 K, while the highest detectable transition is J=90–89 for SiO, which corresponds to an energy around 8400 K. Both species trace the dust formation zone of IRC +10216, and the broad energy ranges involved in their detected transitions permit us to derive the physical properties of the gas and the particular zone in which each species has been formed. This allows us to check the accuracy of chemical thermodynamical equilibrium models and the suggested depletion of SiS and SiO due to accretion onto dust grains.

Key words. Stars: AGB and post-AGB, Stars: mass loss, Stars: circumstellar matter, Stars: carbon, Stars: individual: IRC +10216

1. Introduction

IRC +10216 (CW Leo) is the brightest non-Solar System object in the sky at 5 μm . It is the nearest (D~150 pc, Crosas & Menten 1997) carbon-rich evolved star, and it serves as an archetype for the study of mass loss on the asymptotic giant branch (AGB). The star is losing mass at a rate of $\sim 1\text{--}3 \times 10^{-5} M_{\odot}/\text{yr}$ (Crosas & Menten 1997; Schöier & Olofsson 2000), producing a dense, dusty circumstellar envelope (CSE). To date, more than 60 molecules have been detected in the CSE of IRC +10216 (e.g., Cernicharo et al. 2000; He et al. 2008). Thermodynamic equilibrium and non-equilibrium reactions, photochemical reactions, ion-molecule reactions, and the condensation of dust grains establish the abundance stratifications throughout the envelope. It is likely that IRC +10216 is in an advanced evolutionary stage, marking the transition from an AGB to a planetary nebula (Skinner et al. 1998). A detailed study of its infrared emission spectrum can yield unique information on the thermo-physical and chemical structure of the outflow and on the history of mass loss during this important evolutionary phase.

2. Observations and data reduction

Thanks to its high infrared brightness, IRC +10216 is an ideal target for observation with Herschel (Pilbratt et al. 2010). PACS and SPIRE spectroscopic observations were obtained in the context of the Guaranteed Time Key Programme “Mass-loss of Evolved StarS” (Groenewegen et al., *in prep.*).

The PACS instrument, its in-orbit performance and calibration, and its scientific capabilities are described in Poglitsch et al. (2010). The PACS spectroscopic observations of IRC +10216 consist of full SED scans between 52 and 210 μm obtained in a 3×1 raster, i.e. a pointing on the central object, and two pointings 30'' either side. The observations were performed on 2009 Nov 12 (OD 182). The position angle was 110 degrees. The instrument mode was a non-standard version of the chopnod PACS-SED AOT, used with a large chopper throw (6'). The spectral resolving power varies between 1000 and 4500. A description of the observing mode and of the data reduction process can be found in Royer et al. (2010). The only difference with the data reduction of VY CMa as presented in Royer et al. (2010) is that the ground-based calibration was used for IRC +10216. The estimated calibration uncertainty on the line fluxes is 50 %.

The SPIRE FTS measures the Fourier transform of the source spectrum across short (SSW, 194–313 μm) and long (SLW, 303–671 μm) wavelength bands simultaneously. The FWHM beamwidths of the SSW and SLW arrays vary between 17–19'' and 29–42'' respectively. The source spectrum, including the continuum, is restored by taking the inverse transform of the observed interferogram. The absolute flux calibration uncertainty is 15–20% in the SSW band and 20–30% in the SLW band above 20 cm^{-1} (up to 50% below 20 cm^{-1}). For more details on the SPIRE FTS and its calibration see Griffin et al. (2010) and Swinyard et al. (2010).

IRC +10216 was observed with the high-resolution mode of the SPIRE FTS on the 2009 Nov 19 (OD 189). Twenty repetitions were used, each of which consisted of one forward and one reverse scan of the FTS, with each scan taking 66.6s. The total on-source integration time was therefore 2664s. The unapodized

* Herschel is an ESA space observatory with science instruments provided by European-led Principal Investigator consortia and with important participation from NASA.

spectral resolution is 1.4 GHz (0.048 cm^{-1}), and this is 2.1 GHz (0.07 cm^{-1}) after apodization (using extended Norton-Beer function 1.5; Naylor & Tahic 2007).

PACS and SPIRE photometry observations of IRC +10216 are presented in Ladjal et al. (2010).

3. Results

Currently, more than 500 molecular emission lines have been identified in the PACS and SPIRE spectra of IRC +10216 (see Fig. 1), belonging to 10 different molecules and their isotopologues (^{12}CO , ^{13}CO , C^{18}O , H^{12}CN , H^{13}CN , H_2O , NH_3 , SiS , SiO , CS , C^{34}S , ^{13}CS , C_3 , C_2H , HCl , and H^{37}Cl). The detection of this last molecule is discussed by Cernicharo et al. (2010). In the ISO-LWS spectrum shown in Fig. 1, 57 lines belonging to CO and HCN were identified by Cernicharo et al. (1996). The number of identified lines increases to 280 in the PACS spectrum thanks to its higher spectral resolution. Most of the lines in the PACS and SPIRE spectrum arise from HCN, with the strongest lines from ^{12}CO . HCN is one of the most abundant molecular species in the CSEs of carbon stars (Willacy & Cherchneff 1998) and it is known to show maser action in various vibrational states. The strength of the ^{12}CO lines are diagnostics for the thermophysical structure (see Sect. 3.1). In this paper, we focus on the silicon-bearing molecules SiS and SiO, two refractory species that are formed in the inner envelope. As soon as the temperature of the gas falls below a certain critical value, the molecules can start to condense and form dust grains.

High-J rotational lines have been detected from both molecules. For SiO, 80 rotational transitions in the ground-state from $J = 11-10$ to $J = 90-89$ ($E_{\text{up}} = 8432 \text{ K}$), and 99 lines from $J = 26-25$ to $J = 124-123$ ($E_{\text{up}} = 6678 \text{ K}$) for SiS are clearly detected. From the detected lines, $\sim 45\%$ of both species is unblended (see Table A.2 in the online Appendix, which also lists the detected ^{12}CO and ^{13}CO lines). The emission lines of higher-J transitions and rotational transitions in the first vibrational state are very weak, but their line contribution can be deduced from the theoretical modelling (see Sect. 3.2, and Table A.2). The line formation region of the highest-J lines of SiO (SiS) is within the first $5 R_\star$ ($10 R_\star$), i.e., tracing the recently identified dust formation region (Fonfría et al. 2008).

3.1. Thermophysical structure of the envelope

The large number of optically thick ^{12}CO and optically thin ^{13}CO lines enabled us to perform a tomographical study of the CSE. Properties of the circumstellar gas, such as the kinetic temperature, velocity, and density structure, were determined through a non-local thermodynamic equilibrium (non-LTE) radiative transfer modelling of the ^{12}CO lines. The ^{12}CO lines cover energy levels from $J = 3$ (at 31 K) to $J = 47$ (at 5853 K) and trace the envelope for radii $R < 1 \times 10^{17} \text{ cm}$ ($R < 2000 R_\star$). The GASTRoNOoM code was used to calculate the kinetic temperature and velocity structure in the envelope and to solve the non-LTE radiative transfer equations (Decin et al. 2006, 2010). The rate equations were solved for the ground and first excited vibrational state, with $J_{\text{max}}^{\text{up}} = 60$. The CO line list and collisional rates are discussed in Decin et al. (2010). The terminal velocity was deduced from ground-based observations of low-J ^{12}CO lines (De Beck et al. 2010). The GASTRoNOoM code computes the velocity structure by solving the momentum equation and the temperature structure from the equation expressing the conservation of energy (see Eq. 6 in Decin et al. 2006). However, the resulting temperature was slightly too low beyond

Table 1. Parameters for the best-fit model, where numbers in italics indicate input parameters that have been kept fixed at the given value.

$T_{\text{eff}} [\text{K}]$	2050^a	$\dot{M} [M_\odot/\text{yr}]$	1×10^{-5}
$R_\star [10^{13} \text{ cm}]$	5	$R_{\text{dust}} [R_\star]$	5.6^d
$[\text{CO}/\text{H}_2] [10^{-3}]$	1^b	$^{12}\text{CO}/^{13}\text{CO}$	30
distance [pc]	150^c	$n(\text{SiO})/n(\text{H}_2)$	1×10^{-7}
$v_\infty [\text{km s}^{-1}]$	14.5	$n(\text{SiS})/n(\text{H}_2)$	4×10^{-6}

^aGonzález-Alfonso et al. (2007), ^bZuckerman & Dyck (1986),

^cCrosas & Menten (1997), ^dRidgway & Keady (1988)

$60 R_\star$ to correctly predict the lower excitation ^{12}CO lines, which mainly reflects uncertainties in the gas-grain collisional heating. Therefore, we opted to use $T(R) \propto R^{-0.5}$ for $R > 60 R_\star$.

The best-fit model was determined using the log-likelihood function as described in Decin et al. (2007). The derived (circum)stellar parameters are given in Table 1, the deduced thermodynamical structure is displayed in Fig. 2, and the line predictions are shown in Fig. 1. Specifically, we obtained a mass loss rate of $1 \times 10^{-5} M_\odot/\text{yr}$ (with an uncertainty of a factor 2) and a $^{12}\text{CO}/^{13}\text{CO}$ ratio of $\sim 30 \pm 5$. The latter is on the lower side of the range of $^{12}\text{C}/^{13}\text{C}$ ratios quoted in the literature, going from 20 (Barnes et al. 1977) to 50 (Schöier & Olofsson 2000). The lowest value is obtained from vibra-rotational transitions in the fundamental band of CO, and higher values are often obtained from low-excitation CO or CS lines. The accuracy of isotopologue ratios obtained from low-excitation rotational transitions is often limited by the uncertain effect of photodissociation by interstellar UV photons and chemical fractionation (e.g., Mamajek et al. 1988), effects that are not hampering the high-excitation ^{12}CO and ^{13}CO lines in the PACS and SPIRE spectra.

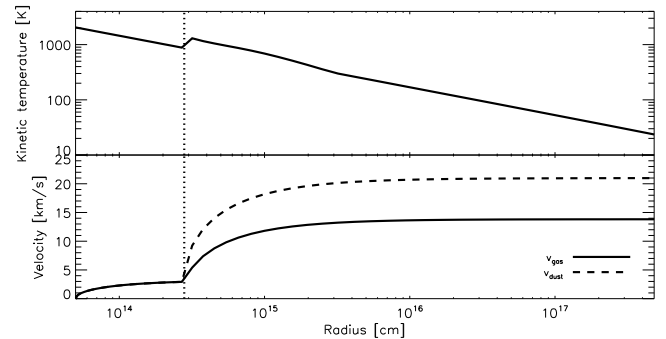


Figure 2. Thermodynamical structure in the envelope of IRC +10216 as derived from the ^{12}CO rotational line transitions. The vertical dotted line represents the dust condensation radius.

3.2. Abundance profiles of SiO and SiS

The SiO and SiS emission lines are modelled with the thermodynamical structure as deduced in Sect. 3.1. Linelists and (available) collisional rates are described in Decin et al. (2010). However, the lack of collisional rates for high-J transitions of both molecules with He or H_2 led us calculate the level populations in LTE. This approach is justified since most of the detected high-J lines originate in the stellar photosphere and in the inner wind envelope, where the high gas density and temperature ensure thermal equilibrium for the level populations. Pulsation driven shocks in the inner envelope may alter abundances pre-

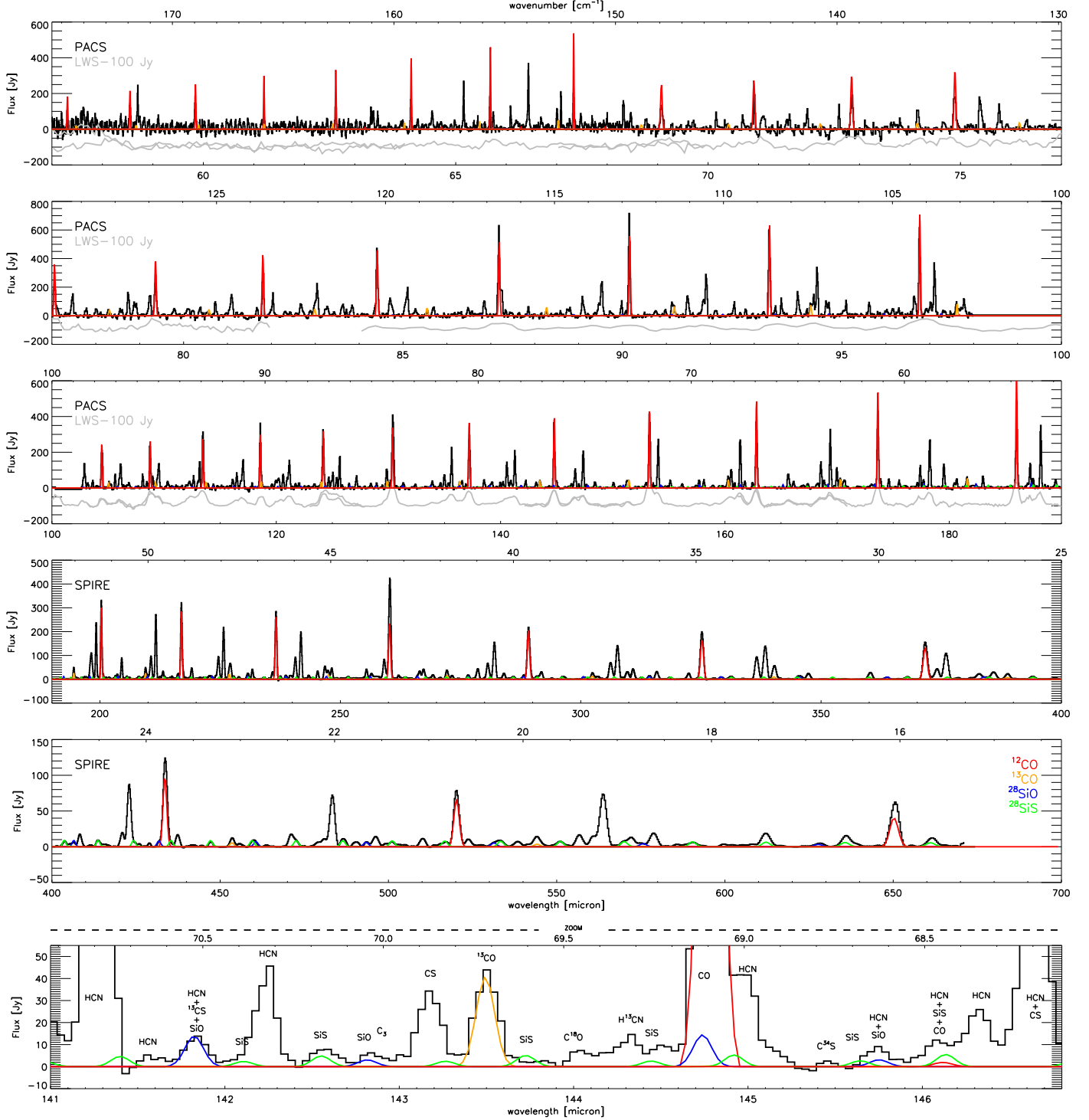


Figure 1. Continuum-subtracted PACS and SPIRE spectrum of IRC +10216. In the three upper panels, the PACS spectrum of IRC +10216 (black) is compared to the ISO-LWS spectrum (grey, Cernicharo et al. 1996). The fourth and fifth panels show the SPIRE spectrum of IRC +10216 (black). The bottom panel zooms in on the 141–146.8 μm region, where we identified the main molecular features. Theoretical line predictions for ^{12}CO (red), ^{13}CO (orange), ^{28}SiO (blue), and ^{28}SiS (green) using the parameters given in Table 1 are displayed in all panels.

dicted from equilibrium chemistry. The estimated uncertainty on the derived abundances is a factor of 5, when taking the line flux uncertainty into account.

SiO : Using an outer radius value of $560 R_{\star}$ (Olofsson et al. 1982), the derived fractional abundance is $[\text{SiO}/\text{H}_2] = 1 \times 10^{-7}$,

when assuming a constant abundance profile. The high-J SiO lines in the PACS and SPIRE spectrum provide us with a diagnostic tool for deducing possible depletion from the gas from accretion onto dust grains. Unfortunately, the low signal-to-noise ratio of the (weak) high-excitation SiO lines prohibit us from putting strong constraints on the role of SiO in the dust forma-

tion around IRC +10216. When allowing for variations in the abundance profile (as described in Decin et al. 2010), we deduce that the SiO fractional abundance in the inner wind ($R \lesssim 8 R_\star$) can range between $0.2 - 3 \times 10^{-7}$, with the fractional abundance being 1×10^{-7} beyond $8 R_\star$ (see Fig. 3). Keady & Ridgway (1993) derived an inner wind SiO abundance of 8×10^{-7} from infrared ro-vibrational transitions. From low-excitation SiO lines, Schöier et al. (2006) obtained an SiO abundance in the region between ~ 3 and $8 R_\star$, as high as $\sim 1.5 \times 10^{-6}$, superposed on a more spatially extended region of $480 R_\star$ with a fractional abundance of 1.7×10^{-7} . The abundance in this compact inner-wind region is a factor 5 higher than our maximum deduced value of 3×10^{-7} in the inner wind. The theoretically calculated photospheric TE value of SiO in carbon-rich envelopes is $\sim 2.8 \times 10^{-8}$ (Willacy & Cherchneff 1998). In their study of the effect of pulsationally induced non-chemical equilibrium in the inner wind of IRC +10216, Willacy & Cherchneff (1998) obtained a fractional abundance of 3.8×10^{-7} . Since TE-value agrees with our minimum deduced value in the inner wind of 2×10^{-8} , and the non-TE value with the maximum deduced value, the effect of pulsationally induced non-equilibrium chemistry is difficult to estimate.

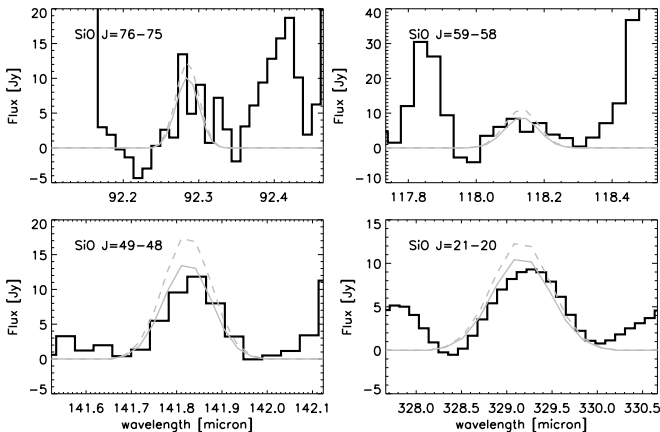


Figure 3. Comparison between few PACS and SPIRE SiO $v=0$ lines (black) and theoretical line predictions (grey). Full grey lines represent theoretical line profiles using a constant SiO fractional abundance of $[SiO/H_2] = 1 \times 10^{-7}$, and dashed grey lines represent model predictions simulating an inner wind abundance of $[SiO/H_2] = 3 \times 10^{-7}$ for $R < 8 R_\star$ and 1×10^{-7} beyond that radius.

SiS: The SiS fractional abundances derived from the PACS and SPIRE observations is $[SiS/H_2] = 4 \times 10^{-6}$. When taking the abundance uncertainty into account, this agrees with the results of Schöier et al. (2007), who find a value of 2×10^{-6} from low-excitation SiS lines. From observations of the $13.5 \mu m$ fundamental band of SiS, Boyle et al. (1994) obtained a gradient in the abundance of SiS, going from 4.3×10^{-6} at a distance of $12 R_\star$ and rising to 4.3×10^{-5} close to the stellar surface. Bieging & Nguyen-Quang-Rieu (1989) obtained a much lower value of $[SiS/H_2] = 7.5 \times 10^{-6}$ for $R < 3 \times 10^{15} \text{ cm}$ and 6.5×10^{-7} beyond that radius. The PACS and SPIRE observations can allow for a change of a factor of 2 in the first few stellar radii (i.e., minimum of 2×10^{-6} , maximum of 8×10^{-6} for $R \lesssim 12 R_\star$). The SiS TE and non-TE inner wind values as computed by Willacy & Cherchneff (1998) are $[SiS/H_2] = 1.5 \times 10^{-5}$ and 3.4×10^{-5} , respectively. That our deduced SiS fractional abundance is clearly lower than the non-TE value of Willacy & Cherchneff

(1998) might indicate toward uncertainties in the estimated rate values in Eqs. (11)-(13) in Willacy & Cherchneff (1998).

4. Conclusion

The PACS and SPIRE spectroscopic observations of IRC +10216 have been shown to be of excellent quality for studying the thermodynamical and chemical structure of the envelope, created by its copious mass loss. The temperature and mass-loss rate of the envelope are derived from the ^{12}CO lines. Both SiO and SiS are refractory species, and the PACS and SPIRE data can provide a strong diagnostic tool for determining their role in the dust formation process. Analysing the high-J SiO and SiS lines yields a constant fractional abundance of 1×10^{-7} and 4×10^{-6} , respectively. However, we detect only $v=0$ and $v=1$ transitions for both species, mainly because of the densely populated spectrum of IRC+10216, while it is known from ground-based observations that levels of SiS up to $v=8$ have been detected (Agúndez et al., 2010, *in prep.*). Moreover, the low-J transitions of SiO and SiS, which are more sensitive to the external envelope, are not accessible to PACS and SPIRE. Since the high-J lines in the ground-state and the $v=1$ lines of both molecules are very weak, we cannot put strong constraints on the fractional abundance in the inner envelope ($R \lesssim 10 R_\star$). For SiO, $1/3$ at most is estimated to take part in dust formation process, while we deduce a fraction of $1/2$ for SiS. Only a merged set of millimeter, submillimeter, and far-infrared observations of SiO and SiS can provide a detailed analysis of the abundance of these species from the photosphere to the photodissociation zone (Agúndez et al., 2010, *in prep.*).

Acknowledgements. PACS was developed by a consortium of institutes led by MPE (Germany) and including UVIE (Austria); KUL, CSL, IMEC (Belgium); CEA, OAMP (France); MPIA (Germany); IFSI, OAP/AOT, OAA/CAISMI, LENS, SISSA (Italy); IAC (Spain). This development has been supported by the funding agencies BMVIT (Austria), ESA-PRODEX (Belgium), CEA/CNES (France), DLR (Germany), ASI (Italy), and CICT/MCT (Spain). SPIRE has been developed by a consortium of institutes led by Cardiff Univ. (UK) and including Univ. Lethbridge (Canada); NAOC (China); CEA, LAM (France); IFSI, Univ. Padua (Italy); IAC (Spain); Stockholm Observatory (Sweden); Imperial College London; RAL, UCL-MSSL, UKATC, Univ. Sussex (UK); Caltech, JPL, NHSC, Univ. Colorado (USA). This development has been supported by national funding agencies: CSA (Canada); NAOC (China); CEA, CNES, CNRS (France); ASI (Italy); MCINN (Spain); SNSB (Sweden); STFC (UK); and NASA (USA). LD acknowledges financial support from the Fund for Scientific Research - Flanders (FWO). MG, DL, JB, WDM, KE, RH, CH, SR, PR, and BV acknowledge support from the Belgian Federal Science Policy Office via the PRODEX Programme of ESA. FK acknowledges funding by the Austrian Science Fund FWF under project number P18939-N16 and I163-N16

References

- Barnes, T. G., Hinkle, K. H., Lambert, D. L., & Beer, R. 1977, ApJ, 213, 71
- Bieging, J. H. & Nguyen-Quang-Rieu. 1989, ApJ, 343, L25
- Boyle, R. J., Keady, J. J., Jennings, D. E., et al. 1994, ApJ, 420, 863
- Cernicharo, J., Barlow, M. J., Gonzalez-Alfonso, E., et al. 1996, A&A, 315, L201
- Cernicharo, J., Decin, L., Barlow, M., & et al. 2010, A&A, this volume
- Cernicharo, J., Guélin, M., & Kahane, C. 2000, A&AS, 142, 181
- Crosas, M. & Menten, K. M. 1997, ApJ, 483, 913
- De Beck, E., Decin, L., de Koter, A., et al. 2010, A&A, accepted for publication
- Decin, L., De Beck, E., Brunken, S., et al. 2010, A&A, in press
- Decin, L., Hony, S., de Koter, A., et al. 2006, A&A, 456, 549
- Decin, L., Hony, S., de Koter, A., et al. 2007, A&A, 475, 233
- Fonfría, J. P., Cernicharo, J., Richter, M. J., & Lacy, J. H. 2008, ApJ, 673, 445
- González-Alfonso, E., Neufeld, D. A., & Melnick, G. J. 2007, ApJ, 669, 412
- Griffin, M. J., Abergel, A., Ade, P. A. R., et al. 2010, A&A, this volume
- He, J. H., Dinh-V-Trung, Kwok, S., et al. 2008, ApJS, 177, 275
- Keady, J. J. & Ridgway, S. T. 1993, ApJ, 406, 199
- Ladjal et al. 2010, A&A, this volume
- Mamon, G. A., Glassgold, A. E., & Huggins, P. J. 1988, ApJ, 328, 797
- Naylor, D. A. & Tahic, M. K. 2007, J. of Optical Soc. of America A, 24, 3644

- Olofsson, H., Johansson, L. E. B., Hjalmarson, A., & Nguyen-Quang-Rieu.
1982, A&A, 107, 128
- Pilbratt, G. L., Riedinger, J. R., Passvogel, T., et al. 2010, A&A, this volume
- Poglitsch, A., Waelkens, C., Geis, N., et al. 2010, A&A, this volume
- Ridgway, S. & Keady, J. J. 1988, ApJ, 326, 843
- Royer, P., Decin, L., & et al. 2010, A&A, this volume
- Schöier, F. L., Bast, J., Olofsson, H., & Lindqvist, M. 2007, A&A, 473, 871
- Schöier, F. L., Fong, D., Olofsson, H., et al. 2006, ApJ, 649, 965
- Schöier, F. L. & Olofsson, H. 2000, A&A, 359, 586
- Skinner, C. J., Meixner, M., & Bobrowsky, M. 1998, MNRAS, 300, L29
- Swinyard, B. M., Ade, P. A. R., Baluteau, J., et al. 2010, A&A, this volume
- Willacy, K. & Cherchneff, I. 1998, A&A, 330, 676
- Zuckerman, B. & Dyck, H. M. 1986, ApJ, 304, 394

¹ Instituut voor Sterrenkunde, Katholieke Universiteit Leuven,
Celestijnenlaan 200D, 3001 Leuven, Belgium
e-mail: Leen.Decin@ster.kuleuven.be

² Sterrenkundig Instituut Anton Pannekoek, University of
Amsterdam, Science Park 904, NL-1098 Amsterdam, The
Netherlands

³ Laboratory of Molecular Astrophysics, Department of
Astrophysics, CAB, INTA-CSIC, Ctra de Ajalvir, km 4, 28850
Torrejón de Ardoz, Madrid Spain

⁴ Dept of Physics & Astronomy, University College London,
Gower St, London WC1E 6BT, UK

⁵ Space Science and Technology Department, Rutherford Appleton
Laboratory, Oxfordshire, OX11 0QX, UK

⁶ Department of Physics, University of Lethbridge, Lethbridge,
Alberta, T1J 1B1, Canada

⁷ Departamento de Astrofísica Molecular e Infrarroja, Instituto de
Estructura de la Materia, CSIC, Serrano 121, 28006 Madrid, Spain

⁸ Radio Astronomy Laboratory, University of California at
Berkeley, CA 94720, USA

⁹ Observatoire de Paris-Meudon, LERMA UMR CNRS 8112, 5
place Jules Janssen, 92195 Meudon Cedex, France

¹⁰ LUTH, Observatoire de Paris-Meudon, 5 Place Jules Janssen,
92190 Meudon, France

¹¹ Max-Planck-Institut für extraterrestrische Physik,
Giessenbachstrasse, 85748, Germany

¹² School of Physics and Astronomy, Cardiff University, Queens
Buildings, The Parade, Cardiff, CF24 3AA, UK

¹³ Royal Observatory of Belgium, Ringlaan 3, B-1180 Brussels,
Belgium

¹⁴ Blue Sky Spectroscopy, 9/740 4 Ave S, Lethbridge, Alberta T1J
ON9, Canada

¹⁵ UK Astronomy Technology Centre, Royal Observatory
Edinburgh, Blackford Hill, Edinburgh EH9 3HJ, UK

¹⁶ Dept of Astronomy, Stockholm University, AlbaNova University
Center, Roslagstullsbacken 21, 10691 Stockholm, Sweden

¹⁷ University of Vienna, Department of Astronomy, Türkenschanz-
straße 17, A-1180 Vienna, Austria

¹⁸ Mullard Space Science Laboratory, University College London,
Holmbury St. Mary, Dorking, Surrey RH5 6NT, UK

**Appendix A: Identified lines of $^{12}\text{C}^{16}\text{O}$, $^{13}\text{C}^{16}\text{O}$,
 $^{28}\text{Si}^{16}\text{O}$, and $^{28}\text{Si}^{32}\text{S}$**

Table A.2. Identified lines of $^{12}\text{C}^{16}\text{O}$, $^{13}\text{C}^{16}\text{O}$, $^{28}\text{Si}^{16}\text{O}$, and $^{28}\text{Si}^{32}\text{S}$ in the PACS and SPIRE spectrum of IRC 10216. The integrated flux values in the fifth column are for the model predictions as shown in Fig. 1. The last column indicates whether a line is blended strongly with another line.

Molecule	Transition	Frequency [GHz]	Wavelength [μm]	Integrated Flux [erg/cm 2 /s]	Blend
$^{12}\text{C}^{16}\text{O}$	v=0-0, J=4-3	461.042	650.250	1.35e-12	no
$^{12}\text{C}^{16}\text{O}$	v=0-0, J=5-4	576.267	520.232	2.20e-12	no
$^{12}\text{C}^{16}\text{O}$	v=0-0, J=6-5	691.474	433.555	3.08e-12	no
$^{12}\text{C}^{16}\text{O}$	v=0-0, J=7-6	806.652	371.650	4.17e-12	no
$^{12}\text{C}^{16}\text{O}$	v=0-0, J=8-7	921.799	325.225	4.98e-12	no
$^{12}\text{C}^{16}\text{O}$	v=0-0, J=9-8	1036.913	289.120	6.01e-12	no
$^{12}\text{C}^{16}\text{O}$	v=0-0, J=10-9	1151.986	260.240	6.67e-12	no
$^{12}\text{C}^{16}\text{O}$	v=0-0, J=11-10	1267.016	236.613	7.22e-12	no
$^{12}\text{C}^{16}\text{O}$	v=0-0, J=12-11	1381.995	216.927	1.98e-12	no
$^{12}\text{C}^{16}\text{O}$	v=0-0, J=13-12	1496.924	200.272	2.99e-12	no
$^{12}\text{C}^{16}\text{O}$	v=0-0, J=14-13	1611.792	185.999	7.36e-12	no
$^{12}\text{C}^{16}\text{O}$	v=0-0, J=15-14	1726.604	173.631	7.31e-12	no
$^{12}\text{C}^{16}\text{O}$	v=0-0, J=16-15	1841.347	162.812	7.32e-12	no
$^{12}\text{C}^{16}\text{O}$	v=0-0, J=17-16	1956.017	153.267	6.95e-12	no
$^{12}\text{C}^{16}\text{O}$	v=0-0, J=18-17	2070.616	144.784	6.68e-12	no
$^{12}\text{C}^{16}\text{O}$	v=0-0, J=19-18	2185.134	137.196	6.47e-12	no
$^{12}\text{C}^{16}\text{O}$	v=0-0, J=20-19	2299.570	130.369	6.15e-12	no
$^{12}\text{C}^{16}\text{O}$	v=0-0, J=21-20	2413.917	124.193	5.88e-12	no
$^{12}\text{C}^{16}\text{O}$	v=0-0, J=22-21	2528.171	118.581	5.53e-12	no
$^{12}\text{C}^{16}\text{O}$	v=0-0, J=23-22	2642.332	113.458	5.08e-12	no
$^{12}\text{C}^{16}\text{O}$	v=0-0, J=24-23	2756.388	108.763	4.83e-12	no
$^{12}\text{C}^{16}\text{O}$	v=0-0, J=25-24	2870.339	104.445	4.51e-12	no
$^{12}\text{C}^{16}\text{O}$	v=0-0, J=27-26	3097.909	96.773	4.06e-12	no
$^{12}\text{C}^{16}\text{O}$	v=0-0, J=28-27	3211.518	93.349	3.85e-12	no
$^{12}\text{C}^{16}\text{O}$	v=0-0, J=29-28	3325.005	90.163	3.55e-12	yes
$^{12}\text{C}^{16}\text{O}$	v=0-0, J=30-29	3438.365	87.190	3.38e-12	yes
$^{12}\text{C}^{16}\text{O}$	v=0-0, J=31-30	3551.594	84.411	3.09e-12	no
$^{12}\text{C}^{16}\text{O}$	v=0-0, J=32-31	3664.685	81.806	2.95e-12	no
$^{12}\text{C}^{16}\text{O}$	v=0-0, J=33-32	3777.637	79.360	2.68e-12	no
$^{12}\text{C}^{16}\text{O}$	v=0-0, J=34-33	3890.443	77.059	2.59e-12	no
$^{12}\text{C}^{16}\text{O}$	v=0-0, J=35-34	4003.102	74.890	2.31e-12	no
$^{12}\text{C}^{16}\text{O}$	v=0-0, J=36-35	4115.605	72.843	2.18e-12	no
$^{12}\text{C}^{16}\text{O}$	v=0-0, J=37-36	4227.953	70.907	2.05e-12	yes
$^{12}\text{C}^{16}\text{O}$	v=0-0, J=38-37	4340.138	69.074	1.89e-12	no
$^{12}\text{C}^{16}\text{O}$	v=0-0, J=39-38	4452.159	67.336	1.74e-12	no
$^{12}\text{C}^{16}\text{O}$	v=0-0, J=40-39	4564.005	65.686	1.60e-12	no
$^{12}\text{C}^{16}\text{O}$	v=0-0, J=41-40	4675.681	64.117	1.50e-12	no
$^{12}\text{C}^{16}\text{O}$	v=0-0, J=42-41	4787.174	62.624	1.34e-12	no
$^{12}\text{C}^{16}\text{O}$	v=0-0, J=43-42	4898.484	61.201	1.31e-12	no
$^{12}\text{C}^{16}\text{O}$	v=0-0, J=44-43	5009.608	59.843	1.18e-12	yes
$^{12}\text{C}^{16}\text{O}$	v=0-0, J=45-44	5120.540	58.547	1.12e-12	no
$^{12}\text{C}^{16}\text{O}$	v=1-1, J=28-27	3182.136	94.211	1.42e-13	yes
$^{12}\text{C}^{16}\text{O}$	v=1-1, J=29-28	3294.573	90.996	1.41e-13	yes
$^{12}\text{C}^{16}\text{O}$	v=1-1, J=30-29	3406.884	87.996	1.51e-13	no
$^{12}\text{C}^{16}\text{O}$	v=1-1, J=31-30	3519.060	85.191	1.48e-13	no
$^{12}\text{C}^{16}\text{O}$	v=1-1, J=32-31	3631.105	82.562	1.51e-13	no
$^{13}\text{C}^{16}\text{O}$	v=0-0, J=5-4	550.926	544.161	1.17e-13	yes
$^{13}\text{C}^{16}\text{O}$	v=0-0, J=6-5	661.066	453.498	1.75e-13	no
$^{13}\text{C}^{16}\text{O}$	v=0-0, J=7-6	771.183	388.743	2.39e-13	yes
$^{13}\text{C}^{16}\text{O}$	v=0-0, J=8-7	881.273	340.181	3.19e-13	yes
$^{13}\text{C}^{16}\text{O}$	v=0-0, J=9-8	991.330	302.414	4.05e-13	no
$^{13}\text{C}^{16}\text{O}$	v=0-0, J=10-9	1101.351	272.204	4.85e-13	no
$^{13}\text{C}^{16}\text{O}$	v=0-0, J=11-10	1211.330	247.490	5.39e-13	no
$^{13}\text{C}^{16}\text{O}$	v=0-0, J=12-11	1321.267	226.898	6.11e-13	yes
$^{13}\text{C}^{16}\text{O}$	v=0-0, J=13-12	1431.152	209.476	6.27e-13	no

Table A.2. continued.

Molecule	Transition	Frequency [GHz]	Wavelength [μm]	Integrated Flux [erg/cm ² /s]	Blend
¹³ C ¹⁶ O	v=0-0, J=14-13	1540.987	194.546	2.91e-13	no
¹³ C ¹⁶ O	v=0-0, J=15-14	1650.768	181.608	6.94e-13	no
¹³ C ¹⁶ O	v=0-0, J=16-15	1760.487	170.290	6.99e-13	no
¹³ C ¹⁶ O	v=0-0, J=17-16	1870.142	160.305	7.05e-13	no
¹³ C ¹⁶ O	v=0-0, J=18-17	1979.728	151.431	7.03e-13	no
¹³ C ¹⁶ O	v=0-0, J=19-18	2089.239	143.494	6.87e-13	no
¹³ C ¹⁶ O	v=0-0, J=20-19	2198.678	136.351	6.68e-13	no
¹³ C ¹⁶ O	v=0-0, J=21-20	2308.034	129.891	6.32e-13	yes
¹³ C ¹⁶ O	v=0-0, J=22-21	2417.308	124.019	6.36e-13	yes
¹³ C ¹⁶ O	v=0-0, J=23-22	2526.492	118.660	5.93e-13	yes
¹³ C ¹⁶ O	v=0-0, J=24-23	2635.584	113.748	5.73e-13	no
¹³ C ¹⁶ O	v=0-0, J=25-24	2744.579	109.231	5.63e-13	no
¹³ C ¹⁶ O	v=0-0, J=26-25	2853.476	105.062	5.39e-13	no
¹³ C ¹⁶ O	v=0-0, J=28-27	3070.949	97.622	4.90e-13	no
¹³ C ¹⁶ O	v=0-0, J=29-28	3179.518	94.289	4.75e-13	no
¹³ C ¹⁶ O	v=0-0, J=30-29	3287.974	91.178	4.58e-13	no
¹³ C ¹⁶ O	v=0-0, J=31-30	3396.307	88.270	4.39e-13	no
¹³ C ¹⁶ O	v=0-0, J=32-31	3504.517	85.545	4.22e-13	no
¹³ C ¹⁶ O	v=0-0, J=33-32	3612.599	82.985	4.11e-13	yes
¹³ C ¹⁶ O	v=0-0, J=34-33	3720.548	80.578	3.97e-13	no
¹³ C ¹⁶ O	v=0-0, J=35-34	3828.359	78.308	3.83e-13	no
¹³ C ¹⁶ O	v=0-0, J=36-35	3936.033	76.166	3.72e-13	no
¹³ C ¹⁶ O	v=0-0, J=37-36	4043.562	74.141	3.63e-13	yes
¹³ C ¹⁶ O	v=0-0, J=38-37	4150.945	72.223	3.54e-13	yes
¹³ C ¹⁶ O	v=0-0, J=39-38	4258.172	70.404	3.52e-13	no
¹³ C ¹⁶ O	v=0-0, J=40-39	4365.246	68.677	3.35e-13	no
¹³ C ¹⁶ O	v=0-0, J=41-40	4472.161	67.035	3.33e-13	no
¹³ C ¹⁶ O	v=0-0, J=42-41	4578.908	65.472	3.11e-13	no
¹³ C ¹⁶ O	v=0-0, J=43-42	4685.490	63.983	3.16e-13	no
¹³ C ¹⁶ O	v=0-0, J=44-43	4791.901	62.562	3.03e-13	no
²⁸ Si ¹⁶ O	v=0-0, J=11-10	477.569	627.746	7.26e-14	no
²⁸ Si ¹⁶ O	v=0-0, J=12-11	520.740	575.705	9.52e-14	no
²⁸ Si ¹⁶ O	v=0-0, J=13-12	564.209	531.350	1.19e-13	no
²⁸ Si ¹⁶ O	v=0-0, J=14-13	607.679	493.340	1.41e-13	no
²⁸ Si ¹⁶ O	v=0-0, J=15-14	650.850	460.617	1.62e-13	no
²⁸ Si ¹⁶ O	v=0-0, J=16-15	694.319	431.779	1.81e-13	no
²⁸ Si ¹⁶ O	v=0-0, J=17-16	737.490	406.504	1.94e-13	no
²⁸ Si ¹⁶ O	v=0-0, J=18-17	780.959	383.877	2.11e-13	no
²⁸ Si ¹⁶ O	v=0-0, J=19-18	824.130	363.769	2.16e-13	no
²⁸ Si ¹⁶ O	v=0-0, J=20-19	867.600	345.542	2.29e-13	no
²⁸ Si ¹⁶ O	v=0-0, J=21-20	910.770	329.164	2.33e-13	no
²⁸ Si ¹⁶ O	v=0-0, J=22-21	953.940	314.268	2.46e-13	no
²⁸ Si ¹⁶ O	v=0-0, J=23-22	997.410	300.571	2.49e-13	no
²⁸ Si ¹⁶ O	v=0-0, J=24-23	1040.580	288.101	2.57e-13	no
²⁸ Si ¹⁶ O	v=0-0, J=25-24	1083.750	276.625	2.57e-13	no
²⁸ Si ¹⁶ O	v=0-0, J=26-25	1126.920	266.028	2.55e-13	no
²⁸ Si ¹⁶ O	v=0-0, J=27-26	1170.090	256.213	2.64e-13	no
²⁸ Si ¹⁶ O	v=0-0, J=28-27	1213.260	247.097	2.66e-13	yes
²⁸ Si ¹⁶ O	v=0-0, J=29-28	1256.430	238.606	2.60e-13	no
²⁸ Si ¹⁶ O	v=0-0, J=30-29	1299.601	230.680	2.66e-13	yes
²⁸ Si ¹⁶ O	v=0-0, J=31-30	1342.471	223.314	2.62e-13	no
²⁸ Si ¹⁶ O	v=0-0, J=32-31	1385.641	216.357	7.17e-14	yes
²⁸ Si ¹⁶ O	v=0-0, J=33-32	1428.811	209.820	2.73e-13	no
²⁸ Si ¹⁶ O	v=0-0, J=34-33	1471.681	203.707	9.86e-14	no
²⁸ Si ¹⁶ O	v=0-0, J=35-34	1514.852	197.902	2.75e-13	yes
²⁸ Si ¹⁶ O	v=0-0, J=36-35	1557.722	192.456	1.22e-13	no

Table A.2. continued.

Molecule	Transition	Frequency [GHz]	Wavelength [μm]	Integrated Flux [erg/cm ² /s]	Blend
²⁸ Si ¹⁶ O	v=0-0, J=37-36	1600.592	187.301	2.75e-13	yes
²⁸ Si ¹⁶ O	v=0-0, J=38-37	1643.762	182.382	2.70e-13	no
²⁸ Si ¹⁶ O	v=0-0, J=39-38	1686.633	177.746	2.73e-13	yes
²⁸ Si ¹⁶ O	v=0-0, J=40-39	1729.503	173.340	2.77e-13	no
²⁸ Si ¹⁶ O	v=0-0, J=41-40	1772.373	169.147	2.75e-13	no
²⁸ Si ¹⁶ O	v=0-0, J=42-41	1814.944	165.180	2.79e-13	no
²⁸ Si ¹⁶ O	v=0-0, J=43-42	1857.814	161.368	2.78e-13	yes
²⁸ Si ¹⁶ O	v=0-0, J=44-43	1900.684	157.729	2.77e-13	yes
²⁸ Si ¹⁶ O	v=0-0, J=45-44	1943.255	154.273	2.69e-13	no
²⁸ Si ¹⁶ O	v=0-0, J=46-45	1986.125	150.943	2.68e-13	no
²⁸ Si ¹⁶ O	v=0-0, J=47-46	2028.696	147.776	2.70e-13	no
²⁸ Si ¹⁶ O	v=0-0, J=48-47	2071.266	144.739	2.73e-13	yes
²⁸ Si ¹⁶ O	v=0-0, J=49-48	2113.837	141.824	2.64e-13	no
²⁸ Si ¹⁶ O	v=0-0, J=50-49	2156.408	139.024	2.69e-13	no
²⁸ Si ¹⁶ O	v=0-0, J=51-50	2198.978	136.333	2.60e-13	yes
²⁸ Si ¹⁶ O	v=0-0, J=52-51	2241.549	133.743	2.62e-13	no
²⁸ Si ¹⁶ O	v=0-0, J=53-52	2283.819	131.268	2.59e-13	yes
²⁸ Si ¹⁶ O	v=0-0, J=54-53	2326.390	128.866	2.48e-13	yes
²⁸ Si ¹⁶ O	v=0-0, J=55-54	2368.661	126.566	2.51e-13	yes
²⁸ Si ¹⁶ O	v=0-0, J=56-55	2410.931	124.347	2.48e-13	yes
²⁸ Si ¹⁶ O	v=0-0, J=57-56	2453.202	122.205	2.43e-13	no
²⁸ Si ¹⁶ O	v=0-0, J=58-57	2495.473	120.135	2.37e-13	yes
²⁸ Si ¹⁶ O	v=0-0, J=59-58	2537.744	118.133	2.27e-13	no
²⁸ Si ¹⁶ O	v=0-0, J=60-59	2580.014	116.198	2.27e-13	yes
²⁸ Si ¹⁶ O	v=0-0, J=61-60	2621.985	114.338	2.23e-13	yes
²⁸ Si ¹⁶ O	v=0-0, J=62-61	2664.256	112.524	2.17e-13	yes
²⁸ Si ¹⁶ O	v=0-0, J=63-62	2706.227	110.779	2.10e-13	no
²⁸ Si ¹⁶ O	v=0-0, J=64-63	2748.198	109.087	2.05e-13	yes
²⁸ Si ¹⁶ O	v=0-0, J=65-64	2790.169	107.446	2.01e-13	no
²⁸ Si ¹⁶ O	v=0-0, J=66-65	2832.140	105.854	1.94e-13	yes
²⁸ Si ¹⁶ O	v=0-0, J=67-66	2874.111	104.308	1.84e-13	yes
²⁸ Si ¹⁶ O	v=0-0, J=68-67	2915.782	102.817	1.80e-13	yes
²⁸ Si ¹⁶ O	v=0-0, J=72-71	3082.467	97.257	1.56e-13	no
²⁸ Si ¹⁶ O	v=0-0, J=73-72	3124.138	95.960	1.52e-13	yes
²⁸ Si ¹⁶ O	v=0-0, J=74-73	3165.809	94.697	1.46e-13	yes
²⁸ Si ¹⁶ O	v=0-0, J=75-74	3207.180	93.475	1.37e-13	yes
²⁸ Si ¹⁶ O	v=0-0, J=76-75	3248.552	92.285	1.34e-13	no
²⁸ Si ¹⁶ O	v=0-0, J=77-76	3289.923	91.124	1.28e-13	yes
²⁸ Si ¹⁶ O	v=0-0, J=78-77	3331.294	89.993	1.19e-13	yes
²⁸ Si ¹⁶ O	v=0-0, J=79-78	3372.666	88.889	1.17e-13	no
²⁸ Si ¹⁶ O	v=0-0, J=80-79	3413.737	87.819	1.13e-13	yes
²⁸ Si ¹⁶ O	v=0-0, J=81-80	3454.809	86.775	1.08e-13	yes
²⁸ Si ¹⁶ O	v=0-0, J=82-81	3496.180	85.749	1.03e-13	yes
²⁸ Si ¹⁶ O	v=0-0, J=83-82	3536.952	84.760	9.76e-14	yes
²⁸ Si ¹⁶ O	v=0-0, J=84-83	3578.024	83.787	9.20e-14	yes
²⁸ Si ¹⁶ O	v=0-0, J=85-84	3619.095	82.836	8.84e-14	yes
²⁸ Si ¹⁶ O	v=0-0, J=86-85	3659.867	81.913	8.23e-14	yes
²⁸ Si ¹⁶ O	v=0-0, J=87-86	3700.639	81.011	8.11e-14	yes
²⁸ Si ¹⁶ O	v=0-0, J=88-87	3741.410	80.128	7.74e-14	yes
²⁸ Si ¹⁶ O	v=0-0, J=89-88	3782.182	79.264	7.36e-14	yes
²⁸ Si ¹⁶ O	v=0-0, J=90-89	3822.654	78.425	7.13e-14	yes
²⁸ Si ¹⁶ O	v=1-1, J=39-38	1674.641	179.019	4.06e-14	yes
²⁸ Si ¹⁶ O	v=1-1, J=40-39	1717.211	174.581	4.28e-14	yes
²⁸ Si ¹⁶ O	v=1-1, J=41-40	1759.782	170.358	4.40e-14	yes
²⁸ Si ¹⁶ O	v=1-1, J=42-41	1802.353	166.334	4.74e-14	no
²⁸ Si ¹⁶ O	v=1-1, J=43-42	1844.923	162.496	4.88e-14	yes

Table A.2. continued.

Molecule	Transition	Frequency [GHz]	Wavelength [μm]	Integrated Flux [erg/cm ² /s]	Blend
²⁸ Si ¹⁶ O	v=1-1, J=44-43	1887.194	158.856	5.15e-14	yes
²⁸ Si ¹⁶ O	v=1-1, J=45-44	1929.764	155.352	5.28e-14	no
²⁸ Si ¹⁶ O	v=1-1, J=46-45	1972.035	152.022	5.48e-14	yes
²⁸ Si ¹⁶ O	v=1-1, J=47-46	2014.606	148.809	5.53e-14	yes
²⁸ Si ¹⁶ O	v=1-1, J=48-47	2056.876	145.751	5.64e-14	yes
²⁸ Si ¹⁶ O	v=1-1, J=49-48	2099.147	142.816	5.82e-14	no
²⁸ Si ³² S	v=0-0, J=26-25	471.608	635.682	1.29e-13	yes
²⁸ Si ³² S	v=0-0, J=27-26	489.713	612.180	1.45e-13	yes
²⁸ Si ³² S	v=0-0, J=28-27	507.813	590.360	1.47e-13	no
²⁸ Si ³² S	v=0-0, J=29-28	525.910	570.045	1.61e-13	no
²⁸ Si ³² S	v=0-0, J=30-29	544.003	551.087	1.61e-13	no
²⁸ Si ³² S	v=0-0, J=31-30	562.091	533.352	1.76e-13	no
²⁸ Si ³² S	v=0-0, J=32-31	580.175	516.728	1.74e-13	no
²⁸ Si ³² S	v=0-0, J=33-32	598.254	501.112	1.85e-13	no
²⁸ Si ³² S	v=0-0, J=34-33	616.328	486.417	1.84e-13	no
²⁸ Si ³² S	v=0-0, J=35-34	634.398	472.562	1.91e-13	no
²⁸ Si ³² S	v=0-0, J=36-35	652.463	459.478	1.93e-13	no
²⁸ Si ³² S	v=0-0, J=37-36	670.522	447.103	1.93e-13	no
²⁸ Si ³² S	v=0-0, J=38-37	688.576	435.380	1.98e-13	no
²⁸ Si ³² S	v=0-0, J=39-38	706.625	424.260	1.93e-13	yes
²⁸ Si ³² S	v=0-0, J=40-39	724.668	413.696	2.00e-13	no
²⁸ Si ³² S	v=0-0, J=41-40	742.705	403.649	2.00e-13	no
²⁸ Si ³² S	v=0-0, J=42-41	760.737	394.082	1.97e-13	no
²⁸ Si ³² S	v=0-0, J=43-42	778.762	384.960	2.03e-13	no
²⁸ Si ³² S	v=0-0, J=44-43	796.782	376.254	2.00e-13	yes
²⁸ Si ³² S	v=0-0, J=45-44	814.795	367.936	1.99e-13	no
²⁸ Si ³² S	v=0-0, J=46-45	832.801	359.981	2.04e-13	yes
²⁸ Si ³² S	v=0-0, J=47-46	850.801	352.365	2.02e-13	no
²⁸ Si ³² S	v=0-0, J=48-47	868.795	345.067	1.98e-13	no
²⁸ Si ³² S	v=0-0, J=49-48	886.781	338.068	2.04e-13	yes
²⁸ Si ³² S	v=0-0, J=50-49	904.760	331.350	2.05e-13	no
²⁸ Si ³² S	v=0-0, J=51-50	922.733	324.896	2.00e-13	yes
²⁸ Si ³² S	v=0-0, J=52-51	940.697	318.692	2.01e-13	no
²⁸ Si ³² S	v=0-0, J=53-52	958.655	312.722	2.06e-13	no
²⁸ Si ³² S	v=0-0, J=54-53	976.605	306.974	2.07e-13	yes
²⁸ Si ³² S	v=0-0, J=55-54	994.547	301.436	2.05e-13	no
²⁸ Si ³² S	v=0-0, J=56-55	1012.481	296.097	2.01e-13	no
²⁸ Si ³² S	v=0-0, J=57-56	1030.407	290.946	2.03e-13	no
²⁸ Si ³² S	v=0-0, J=58-57	1048.325	285.973	2.07e-13	no
²⁸ Si ³² S	v=0-0, J=59-58	1066.235	281.169	2.09e-13	yes
²⁸ Si ³² S	v=0-0, J=60-59	1084.136	276.527	2.09e-13	no
²⁸ Si ³² S	v=0-0, J=61-60	1102.029	272.037	2.09e-13	yes
²⁸ Si ³² S	v=0-0, J=62-61	1119.913	267.693	2.08e-13	yes
²⁸ Si ³² S	v=0-0, J=63-62	1137.788	263.487	2.07e-13	no
²⁸ Si ³² S	v=0-0, J=64-63	1155.654	259.414	2.06e-13	yes
²⁸ Si ³² S	v=0-0, J=65-64	1173.511	255.466	2.05e-13	yes
²⁸ Si ³² S	v=0-0, J=66-65	1191.358	251.639	2.04e-13	no
²⁸ Si ³² S	v=0-0, J=67-66	1209.196	247.927	2.04e-13	yes
²⁸ Si ³² S	v=0-0, J=68-67	1227.025	244.325	2.04e-13	no
²⁸ Si ³² S	v=0-0, J=69-68	1244.843	240.827	2.04e-13	yes
²⁸ Si ³² S	v=0-0, J=70-69	1262.652	237.431	2.05e-13	no
²⁸ Si ³² S	v=0-0, J=71-70	1280.451	234.130	2.05e-13	no
²⁸ Si ³² S	v=0-0, J=72-71	1298.240	230.922	2.06e-13	yes
²⁸ Si ³² S	v=0-0, J=73-72	1316.018	227.803	2.05e-13	no
²⁸ Si ³² S	v=0-0, J=74-73	1333.786	224.768	2.04e-13	yes
²⁸ Si ³² S	v=0-0, J=75-74	1351.543	221.815	2.00e-13	no
²⁸ Si ³² S	v=0-0, J=76-75	1369.290	218.940	4.81e-14	yes

Table A.2. continued.

Molecule	Transition	Frequency [GHz]	Wavelength [μm]	Integrated Flux [erg/cm ² /s]	Blend
²⁸ Si ³² S	v=0-0, J=77-76	1387.025	216.141	1.96e-13	yes
²⁸ Si ³² S	v=0-0, J=78-77	1404.750	213.413	5.78e-14	no
²⁸ Si ³² S	v=0-0, J=79-78	1422.463	210.756	1.97e-13	yes
²⁸ Si ³² S	v=0-0, J=80-79	1440.165	208.165	6.35e-14	no
²⁸ Si ³² S	v=0-0, J=81-80	1457.856	205.639	6.63e-14	no
²⁸ Si ³² S	v=0-0, J=82-81	1475.535	203.175	7.07e-14	no
²⁸ Si ³² S	v=0-0, J=83-82	1493.202	200.772	7.24e-14	yes
²⁸ Si ³² S	v=0-0, J=84-83	1510.858	198.425	1.83e-13	yes
²⁸ Si ³² S	v=0-0, J=85-84	1528.501	196.135	7.80e-14	no
²⁸ Si ³² S	v=0-0, J=86-85	1546.132	193.898	1.79e-13	no
²⁸ Si ³² S	v=0-0, J=87-86	1563.751	191.714	8.13e-14	no
²⁸ Si ³² S	v=0-0, J=88-87	1581.357	189.579	1.78e-13	yes
²⁸ Si ³² S	v=0-0, J=89-88	1598.951	187.493	1.71e-13	yes
²⁸ Si ³² S	v=0-0, J=90-89	1616.532	185.454	1.72e-13	no
²⁸ Si ³² S	v=0-0, J=91-90	1634.100	183.460	1.72e-13	no
²⁸ Si ³² S	v=0-0, J=92-91	1651.655	181.510	1.66e-13	yes
²⁸ Si ³² S	v=0-0, J=93-92	1669.197	179.603	1.65e-13	yes
²⁸ Si ³² S	v=0-0, J=94-93	1686.725	177.736	1.60e-13	yes
²⁸ Si ³² S	v=0-0, J=95-94	1704.240	175.910	1.60e-13	no
²⁸ Si ³² S	v=0-0, J=96-95	1721.742	174.122	1.55e-13	no
²⁸ Si ³² S	v=0-0, J=97-96	1739.229	172.371	1.55e-13	no
²⁸ Si ³² S	v=0-0, J=98-97	1756.703	170.656	1.53e-13	yes
²⁸ Si ³² S	v=0-0, J=99-98	1774.163	168.977	1.48e-13	yes
²⁸ Si ³² S	v=0-0, J=100-99	1791.608	167.331	1.44e-13	yes
²⁸ Si ³² S	v=0-0, J=101-100	1809.039	165.719	1.42e-13	yes
²⁸ Si ³² S	v=0-0, J=102-101	1826.456	164.139	1.41e-13	no
²⁸ Si ³² S	v=0-0, J=103-102	1843.858	162.590	1.36e-13	yes
²⁸ Si ³² S	v=0-0, J=104-103	1861.245	161.071	1.31e-13	no
²⁸ Si ³² S	v=0-0, J=105-104	1878.618	159.581	1.32e-13	no
²⁸ Si ³² S	v=0-0, J=106-105	1895.975	158.120	1.27e-13	yes
²⁸ Si ³² S	v=0-0, J=107-106	1913.318	156.687	1.26e-13	no
²⁸ Si ³² S	v=0-0, J=108-107	1930.644	155.281	1.19e-13	yes
²⁸ Si ³² S	v=0-0, J=109-108	1947.956	153.901	1.17e-13	yes
²⁸ Si ³² S	v=0-0, J=110-109	1965.251	152.547	1.13e-13	no
²⁸ Si ³² S	v=0-0, J=111-110	1982.531	151.217	1.15e-13	yes
²⁸ Si ³² S	v=0-0, J=112-111	1999.795	149.912	1.08e-13	yes
²⁸ Si ³² S	v=0-0, J=113-112	2017.043	148.630	1.06e-13	no
²⁸ Si ³² S	v=0-0, J=114-113	2034.275	147.371	1.03e-13	yes
²⁸ Si ³² S	v=0-0, J=115-114	2051.491	146.134	1.03e-13	no
²⁸ Si ³² S	v=0-0, J=116-115	2068.690	144.919	1.00e-13	yes
²⁸ Si ³² S	v=0-0, J=117-116	2085.872	143.725	9.45e-14	no
²⁸ Si ³² S	v=0-0, J=118-117	2103.037	142.552	9.44e-14	no
²⁸ Si ³² S	v=0-0, J=119-118	2120.186	141.399	9.06e-14	yes
²⁸ Si ³² S	v=0-0, J=120-119	2137.318	140.266	8.85e-14	yes
²⁸ Si ³² S	v=0-0, J=121-120	2154.432	139.151	8.56e-14	yes
²⁸ Si ³² S	v=0-0, J=122-121	2171.529	138.056	8.17e-14	no
²⁸ Si ³² S	v=0-0, J=123-122	2188.609	136.979	7.89e-14	yes
²⁸ Si ³² S	v=0-0, J=124-123	2205.671	135.919	7.78e-14	yes
²⁸ Si ³² S	v=1-1, J=50-49	900.341	332.977	3.26e-14	yes
²⁸ Si ³² S	v=1-1, J=51-50	918.224	326.491	3.48e-14	no
²⁸ Si ³² S	v=1-1, J=52-51	936.101	320.257	3.69e-14	no
²⁸ Si ³² S	v=1-1, J=53-52	953.970	314.258	3.89e-14	yes
²⁸ Si ³² S	v=1-1, J=54-53	971.831	308.482	4.08e-14	yes
²⁸ Si ³² S	v=1-1, J=55-54	989.685	302.917	4.28e-14	yes
²⁸ Si ³² S	v=1-1, J=56-55	1007.530	297.552	4.47e-14	no
²⁸ Si ³² S	v=1-1, J=57-56	1025.368	292.376	4.67e-14	yes
²⁸ Si ³² S	v=1-1, J=58-57	1043.197	287.378	4.86e-14	no

Table A.2. continued.

Molecule	Transition	Frequency [GHz]	Wavelength [μm]	Integrated Flux [erg/cm ² /s]	Blend
²⁸ Si ³² S	v=1-1, J=59-58	1061.018	282.552	5.03e-14	yes
²⁸ Si ³² S	v=1-1, J=60-59	1078.831	277.886	5.21e-14	yes
²⁸ Si ³² S	v=1-1, J=61-60	1096.635	273.375	5.37e-14	yes
²⁸ Si ³² S	v=1-1, J=62-61	1114.430	269.010	5.51e-14	yes
²⁸ Si ³² S	v=1-1, J=63-62	1132.217	264.784	5.61e-14	yes
²⁸ Si ³² S	v=1-1, J=64-63	1149.994	260.690	5.68e-14	yes
²⁸ Si ³² S	v=1-1, J=65-64	1167.763	256.724	5.84e-14	yes
²⁸ Si ³² S	v=1-1, J=66-65	1185.522	252.878	6.09e-14	yes
²⁸ Si ³² S	v=1-1, J=67-66	1203.271	249.148	6.29e-14	yes
²⁸ Si ³² S	v=1-1, J=68-67	1221.011	245.528	6.42e-14	yes
²⁸ Si ³² S	v=1-1, J=69-68	1238.741	242.014	6.46e-14	yes
²⁸ Si ³² S	v=1-1, J=70-69	1256.461	238.601	6.40e-14	yes
²⁸ Si ³² S	v=1-1, J=71-70	1274.171	235.284	6.70e-14	no
²⁸ Si ³² S	v=1-1, J=72-71	1291.871	232.061	6.87e-14	yes
²⁸ Si ³² S	v=1-1, J=73-72	1309.561	228.926	6.86e-14	yes
²⁸ Si ³² S	v=1-1, J=74-73	1327.240	225.877	6.86e-14	yes
²⁸ Si ³² S	v=1-1, J=75-74	1344.908	222.909	7.11e-14	yes
²⁸ Si ³² S	v=1-1, J=76-75	1362.566	220.021	1.68e-14	no
²⁸ Si ³² S	v=1-1, J=77-76	1380.213	217.207	1.84e-14	yes
²⁸ Si ³² S	v=1-1, J=78-77	1397.849	214.467	2.06e-14	yes
²⁸ Si ³² S	v=1-1, J=79-78	1415.473	211.797	2.16e-14	yes
²⁸ Si ³² S	v=1-1, J=80-79	1433.086	209.194	7.36e-14	yes
²⁸ Si ³² S	v=1-1, J=81-80	1450.688	206.655	2.50e-14	no
²⁸ Si ³² S	v=1-1, J=82-81	1468.278	204.180	2.65e-14	yes
²⁸ Si ³² S	v=1-1, J=83-82	1485.857	201.764	2.78e-14	yes
²⁸ Si ³² S	v=1-1, J=84-83	1503.423	199.407	2.93e-14	yes
²⁸ Si ³² S	v=1-1, J=85-84	1520.978	197.105	7.32e-14	yes
²⁸ Si ³² S	v=1-1, J=86-85	1538.520	194.858	3.18e-14	yes
²⁸ Si ³² S	v=1-1, J=87-86	1556.050	192.662	3.18e-14	no
²⁸ Si ³² S	v=1-1, J=88-87	1573.567	190.518	7.40e-14	no
²⁸ Si ³² S	v=1-1, J=89-88	1591.072	188.422	7.36e-14	yes
²⁸ Si ³² S	v=1-1, J=90-89	1608.564	186.373	7.34e-14	no
²⁸ Si ³² S	v=1-1, J=91-90	1626.043	184.369	7.26e-14	no
²⁸ Si ³² S	v=1-1, J=92-91	1643.509	182.410	7.13e-14	yes
²⁸ Si ³² S	v=1-1, J=93-92	1660.962	180.493	7.07e-14	yes
²⁸ Si ³² S	v=1-1, J=94-93	1678.402	178.618	7.18e-14	no
²⁸ Si ³² S	v=1-1, J=95-94	1695.828	176.782	6.93e-14	no
²⁸ Si ³² S	v=1-1, J=96-95	1713.240	174.986	6.97e-14	no
²⁸ Si ³² S	v=1-1, J=97-96	1730.639	173.226	6.67e-14	yes
²⁸ Si ³² S	v=1-1, J=98-97	1748.024	171.504	6.84e-14	no
²⁸ Si ³² S	v=1-1, J=99-98	1765.394	169.816	6.79e-14	yes
²⁸ Si ³² S	v=1-1, J=100-99	1782.751	168.163	6.66e-14	yes
²⁸ Si ³² S	v=1-1, J=101-100	1800.093	166.543	6.38e-14	no
²⁸ Si ³² S	v=1-1, J=102-101	1817.420	164.955	6.52e-14	no
²⁸ Si ³² S	v=1-1, J=103-102	1834.733	163.398	6.21e-14	no
²⁸ Si ³² S	v=1-1, J=104-103	1852.032	161.872	6.32e-14	yes
²⁸ Si ³² S	v=1-1, J=105-104	1869.315	160.376	6.08e-14	yes
²⁸ Si ³² S	v=1-1, J=106-105	1886.583	158.908	6.00e-14	yes
²⁸ Si ³² S	v=1-1, J=107-106	1903.836	157.468	6.00e-14	yes
²⁸ Si ³² S	v=1-1, J=108-107	1921.074	156.055	5.87e-14	yes
²⁸ Si ³² S	v=1-1, J=109-108	1938.296	154.668	5.77e-14	yes